Appendix

A.1 EUV OPTICAL CONSTANTS 256

A.2 EUV OPTICAL SYSTEMS 258

A.3 REFLECTIVE MULTILAYER COATINGS FOR EUV 259
    A.3.1 Fabrication Tolerances

A.4 FRESNEL ZONEPLATE LENSES 263

A.5 FRINGE CONTRAST AND MODULATION 265

A.6 FOURIER-TRANSFORM METHOD OF FRINGE CONTRAST DETERMINATION 266

A.7 READING ZERNIKE COEFFICIENT PLOTS 268

A.1 EUV OPTICAL CONSTANTS

The EUV region of the spectrum (nominally 5-20-nm wavelength, or 50-200 eV) is characterized by high absorption in all materials. An empirical understanding of the interaction of EUV light and matter begins with the complex index of refraction. Since the index is close to unity for all materials across the EUV spectral range, a convenient notation is used:

$$n = 1 - \delta + i\beta \tag{1}$$

δ and β are real, empirical constants that have been measured and tabulated for a vast range of materials, over a broad range of wavelengths (Henke et al. 1992). δ represents the *refractive component* of the index, and β is the *extinction coefficient*, related to the absorptivity of the material. The propagation of plane-wave monochromatic light within an isotropic and homogeneous material may be expressed for an arbitrary polarization component as a scalar electric field amplitude E, oscillating with angular frequency ω and initial field amplitude E_o.

$$E(\mathbf{r},t) = E_o e^{-i(\omega t - \mathbf{k}\cdot\mathbf{r})} \, . \tag{2}$$

The phase velocity may be expressed in terms of the magnitude of the wavevector **k** and the complex index of refraction

$$v_{phase} = \frac{\omega}{k} = \frac{c}{n} = \frac{c}{1-\delta+i\beta} \, . \tag{3}$$

Thus

$$k = \frac{\omega}{c} n = \frac{\omega}{c}(1-\delta+i\beta) \, . \tag{4}$$

Using the translational invariance of the plane wave field, perpendicular to the propagation direction, we define **k** in the x-direction and define $\mathbf{r} = x\hat{\mathbf{x}}$. Thus, $\mathbf{k}\cdot\mathbf{r} = kx$, and we have a one-dimensional representation of the field

$$E(\mathbf{r},t) = E(x,t) \, . \tag{5a}$$

$$E(x,t) = E_o \exp\left\{-i\left[\omega t - \frac{\omega}{c}(1-\delta+i\beta)x\right]\right\} \tag{5b}$$

$$= E_o \exp\left[-i\omega t + i\tfrac{2\pi}{\lambda}x\right] \exp\left[-i\tfrac{2\pi}{\lambda}\delta x\right] \exp\left[-\tfrac{2\pi}{\lambda}\beta x\right] \tag{5c}$$

$$= E_o \exp(-i\omega t) \exp\left[i\tfrac{2\pi}{\lambda}(1-\delta)x\right] \exp\left[-\tfrac{2\pi}{\lambda}\beta x\right] . \tag{5d}$$

λ is the free-space wavelength. The extinction in material is described by the electric field intensity

$$I(x) = n\left|E(x,t)\right|^2 \equiv I(0)\exp\left[-\tfrac{4\pi}{\lambda}\beta x\right] . \tag{6}$$

The $1/e$ intensity transmission depth, or *absorption length*, is

$$x_{\frac{1}{e}} \equiv l_{abs} \equiv \frac{1}{4\pi\beta} \, . \tag{7}$$

An analogous depth may be defined to describe the length of material required to produce a phase change

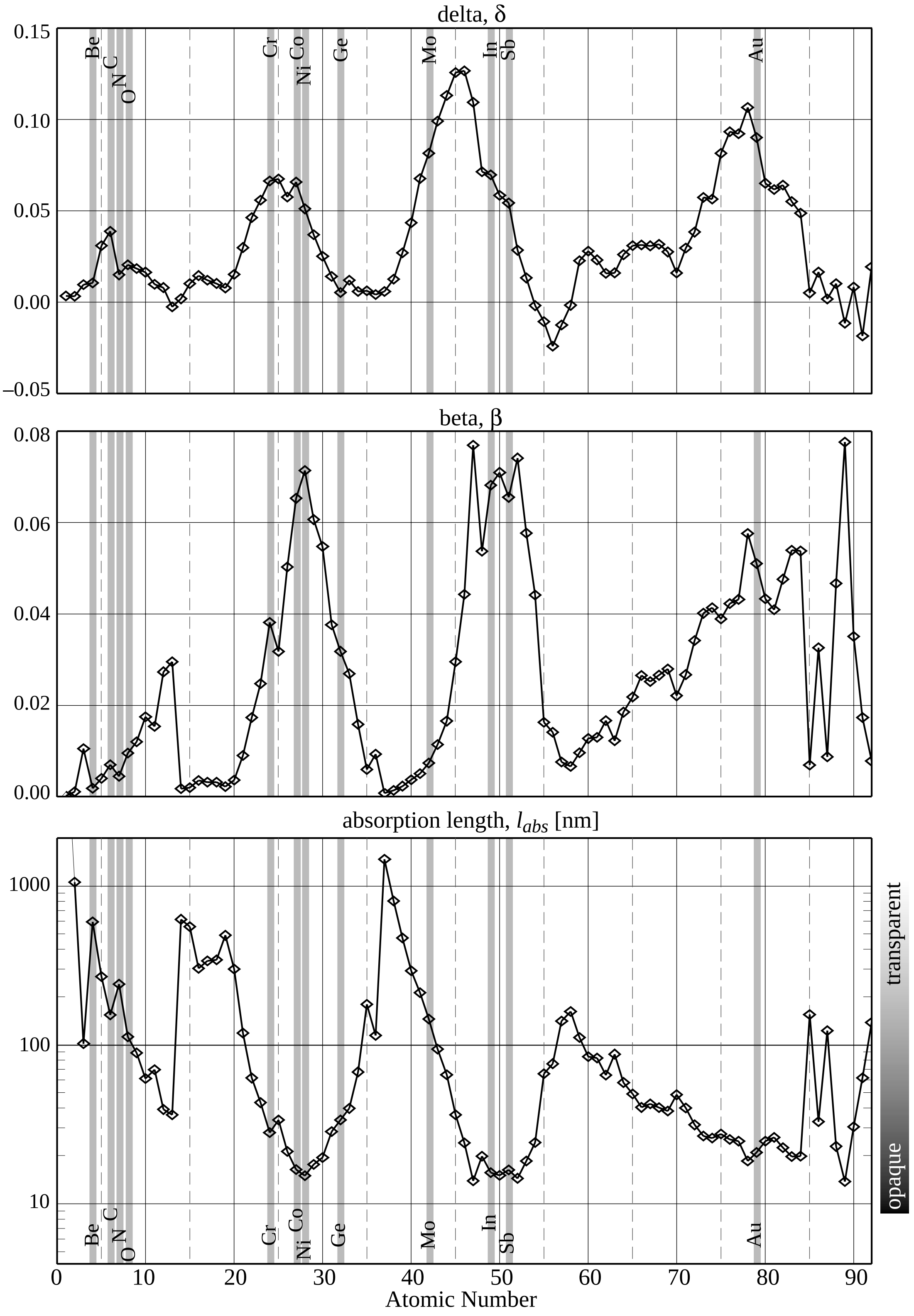

Figure 1. Optical properties of elemental solids at 13.4 nm wavelength (92.5 eV). The index of refraction *n* is defined in terms of the refractive, *real* component $1 - \delta$ and the absorptive, *imaginary* component $i\beta$. The absorption length l_{abs}, defined as the $1/e$ intensity transmission depth, is inversely related to β.

Table 1. Optical properties of selected materials commonly used in EUV applications at 13.4 nm wavelength.

Material	density, ρ [g/cm^3]	δ	β	l_{abs} [nm]
Ag	10.5	0.110161	0.0772735	13.8
Ni	8.902	0.051499	0.0716041	14.9
InSb	7.31	0.064686	0.0699965	15.2
In	7.31	0.070171	0.0682527	15.6
Sb	6.691	0.054474	0.0655745	16.3
Co	8.9	0.066056	0.0653061	16.3
Cr	7.19	0.066673	0.0381981	27.9
Ge	5.323	0.005387	0.0318920	33.4
Si_3N_4	3.44	0.025675	0.0091366	116.7
Mo	10.22	0.076553	0.0073536	145.0
C*	2.2	0.037853	0.0067466	158.1
Si	2.33	0.000069	0.0018211	585.5
Be	1.848	0.010844	0.0017982	593.0
O_2*	1.43×10^{-3}	0.000026	0.0000119	89524.7
N_2*	1.25×10^{-3}	0.000023	0.0000068	155741.6

* Carbon density is given for graphite. Oxygen and nitrogen densities are for the gas-phase at STP.

of 2π relative to vacuum propagation. By inspection, from Eq. 5(d) this phase length is given by

$$x_{2\pi} \equiv l_{phase} \equiv \frac{\lambda}{d} \, . \tag{8}$$

Figure 1 shows the real and imaginary components of the index of refraction for a wide range of elemental solids at 13.4 nm wavelength (92.5 eV). Several materials commonly used in EUV applications are highlighted in the figure, and are listed in Table 1, also for 13.4 nm wavelength.

A.2 EUV OPTICAL SYSTEMS

In general, optical imaging systems function by generating an optical path-length-difference between rays travelling separate paths. There are numerous strategies employed in generating the path-length-difference; the most important to consider are *refractive, reflective,* and *diffractive* systems. This brief section addresses the application of these strategies to EUV wavelengths.

Refractive optics exploit the difference of the refractive index of one material relative to another (or to vacuum) to achieve an optical path-length-difference. Because of the strong absorption at EUV wavelengths for all materials, refractive optical systems pay much too high a price in intensity attenuation to achieve a small change in path length. With the exception of a few limited cases (including phase-shifting elements), refractive optics at EUV wavelengths are not feasible.

Reflective elements for EUV optical systems fall into two main categories: glancing incidence optics, which exploit the phenomena of *total external reflection*, and multilayer optics, which function by creating a resonant standing-wave field in a thin-film stack.

Glancing incidence optical systems are widely used in EUV, soft X-ray, and hard X-ray applications. They possess several advantages for special applications and are invaluable components of synchrotron beamlines. Often comprised of thin substrates bent or polished into a curved profile, glancing incidence optics exploit the high EUV reflectivities that can be achieved when the glancing angles of incidence are limited to a narrow range above zero. Since the real part of the index of refraction is *less than one* for many materials in this energy regime, the phenomenon of high glancing-incidence reflectivity is most easily understood as a *total internal reflection* but with the light propagating in vacuum or air.

Below the *critical angle* of incidence θ_c, defined from the plane of the interface, very high reflectivities may be achieved. θ_c is the angle at and below which the incident field does not propagate into the medium, but rather propagates along the interface. For EUV and X-ray materials for which δ and β are small,

$$\theta_c = (2\delta)^{1/2}. \tag{9}$$

By distributing the incident light over large surface areas, glancing incidence optical systems demonstrate strong advantages in high-incident-power applications such as synchrotron beamlines. The profiles of the optical surfaces are vulnerable to thermal expansion, making cooling an issue of critical importance. By water-cooling the optical substrates and holders, heat from the absorbed power can be removed.

Multilayer-coatings designed for high-reflectivity at near-normal incidence *are* the key enabling technology that has led to the development of EUV lithography as a viable candidate for the 0.1 µm generation of circuit fabrication and beyond. These systems rely heavily on state-of-the-art optical surface figuring and polishing, and on the development of an optical-coating deposition capability that meets the extraordinarily strict tolerances inherent in these systems. Yet multilayer-coatings provide the freedom to design very sophisticated large-scale optical systems with high-resolution over a large field of view, as is required in lithographic applications. Some important properties of multilayers are addressed in Appendix A.3.

While glancing-incidence reflective optics dominate high-incident-power applications, multilayer systems are currently being developed to address the requirements of lithography. High-resolution EUV applications are now dominated by diffractive optics such as Fresnel zoneplate lenses. Created holographically or, more commonly, by taking advantage of other high-resolution lithographic techniques such as electron-beam lithography, these patterned elements typically function as the hologram of a simple singlet lens. The principles of Fresnel zoneplate operation are described in Appendix A.4.

A.3 REFLECTIVE MULTILAYER COATINGS FOR EUV

Multilayer reflection is a resonance phenomenon. When the wavelength, angle, and polarization of the incident field match the resonance conditions determined by the bi-layer period, layer thicknesses and optical properties of the two materials in the multilayer, strong EUV reflectivities may be achieved, *even* *though the materials are highly absorptive* (Stearns et al. 1993). At resonance (peak reflectivity), a standing wave is formed matching the period of the multilayers. Typically the node is formed within the absorptive material and the anti-node within the less-absorptive material. Conditions for high reflectivity exploit the index of refraction *difference* between two materials; the best multilayer material pairs are those for which index difference is large yet neither material is highly absorptive. The materials pair that has been most widely used for EUV near-normal-incidence multilayers near 13-nm wavelength are molybdenum and silicon.

The very resonance properties that enable multilayers to function at normal incidence with high EUV reflectivity also subject them to *extreme* sensitivity to fabrication errors. When the conditions for resonance are not met, the reflected intensity suffers. Of equal or possibly *greater* importance to high-performance imaging systems is the change of phase experienced by the reflected wave. As described in this appendix, even small changes in the multilayer period, or *d-spacing*, can have a dramatic impact on the reflected phase in systems designed for diffraction-limited performance.

To illustrate this extreme sensitivity, the dependence of the reflected intensity and phase of 13.4-nm-wavelength light were calculated and are shown in Fig. 2. (The reflection-phase is shown *relative* to the phase at peak reflectivity.) These simple calculations are based on the method described by Born and Wolf (1980:51-70) for periodically stratified media, with 40 Mo/Si layer pairs. Although the individual layers are approximately only 15 atoms thick, and interfacial diffusion cannot be avoided, the naïve assumption of perfectly abrupt interfaces made in these calculations does not change the outcome significantly.

The optimal layer thicknesses were determined empirically by the author based on normal-incidence reflectivity, using the optical constants recommended by Erik Gullikson (personal communication). The individual layer thicknesses were 4.125 nm of Si and 2.722 nm of Mo. The total bi-layer period d_o is 6.847 nm, and the ratio γ of Mo thickness to the total bi-layer thickness is 0.3975. The peak normal-incidence reflectivity is calculated to be 71.8%.

In the top row of Fig. 2, the multilayer-reflection properties are shown near normal incidence. Dependence on wavelength, layer thickness, and angle are shown. $\Delta d/d_o$ represents a uniform, fractional change in layer thickness about the optimal value. The most significant phase effect that is evident in these plots is the reflected phase change of π-radians that occurs as the parameter under consideration passes through resonance. Across the resonance peak, the phase-dependence is nearly linear with an approximate slope of π divided by the width of the peak.

Two useful empirical formulas describe the phase-dependence near peak reflectivity.

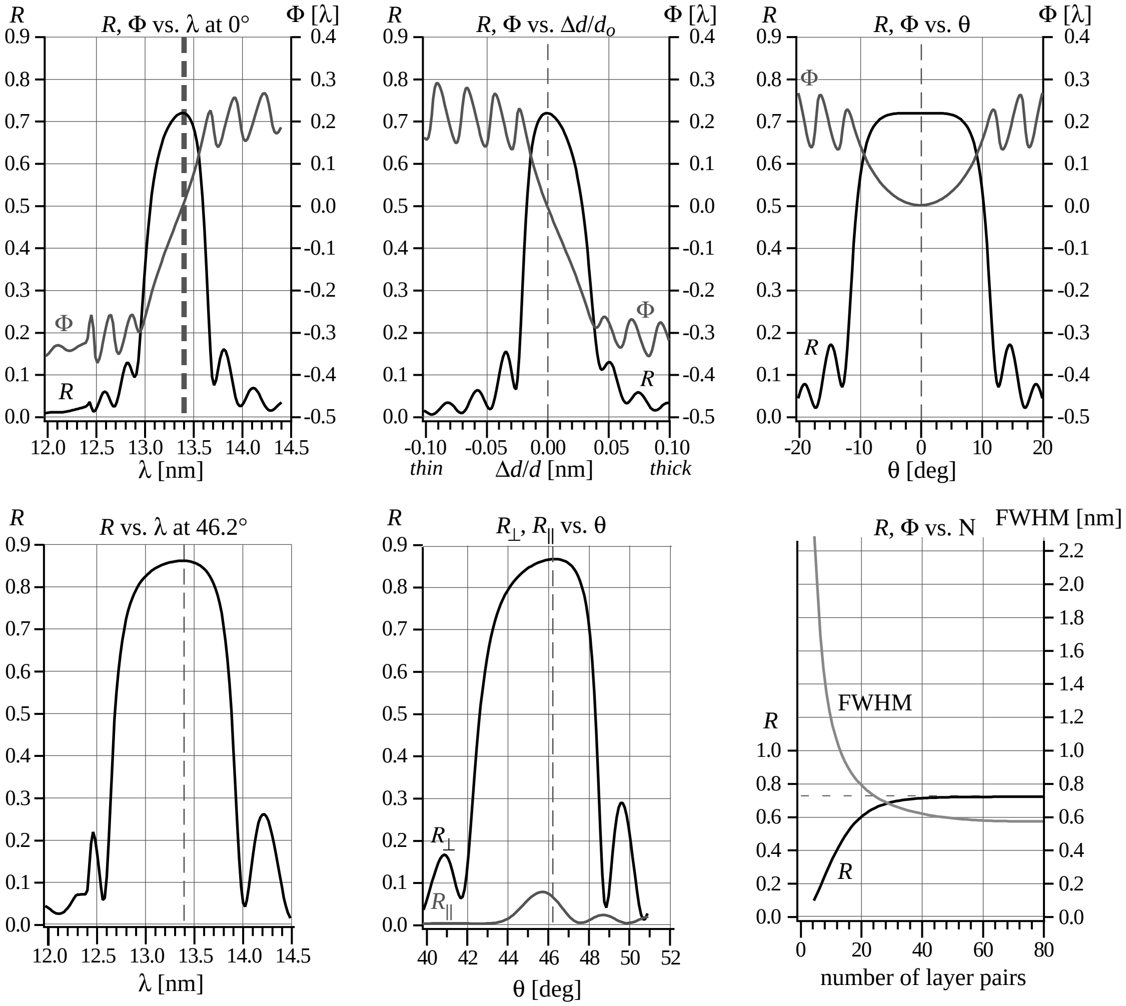

Figure 2. Ideal reflection properties of Mo/Si multilayer mirrors at normal incidence and 46.2° incidence for 13.4 nm wavelength. Optical properties and layer thicknesses are given in the text.

- Dependence of the reflected phase ϕ on incidence angle θ:

$$\phi \text{ [waves]} \approx 1.24\times10^{-3}\, \theta^2 \text{ [deg}^2\text{]}. \tag{10}$$

- Dependence of the reflected phase ϕ on layer thickness error $\Delta d/d_o$:

$$\phi \text{ [waves]} \approx -7.49\, (\Delta d/d_o). \tag{11}$$

Equation (10) is given to demonstrate the magnitude of the angular phase dependence near normal incidence. For most practical purposes, *true* normal-incidence mirrors are of little use — reflective imaging systems *must* contain a finite angle of incidence and a range of angles related to the curvature and size of the surfaces.

The first two graphs of the second row of Fig. 2 model the behavior of the near-45° turning mirror that deflects light vertically toward the object plane of the Schwarzschild objective. The design angle of incidence is 46.2°, and the Mo/Si mirror has 20 layer pairs. The polarizing property of this mirror is evident in the large difference between the *perpendicular* (TE) and the *parallel* (TM) component reflectivities. The last graph of the lower row shows the dependence of the reflectivity and the full-width at half-maximum bandwidth ($\Delta\lambda$) on the number of layer pairs.

A.3.1 *Fabrication Tolerances*

The tight wavefront tolerances of lithographic-quality EUV imaging systems place extremely high demands on the fabrication of the optical substrates and on the deposition of the multilayers. Small layer thickness errors become multiplied by the number of layer pairs to create larger effects. It is an important and revealing exercise to consider the separate contributions of the geometric path-length-change with the change in phase upon reflection that occurs when the layer thickness is varied.

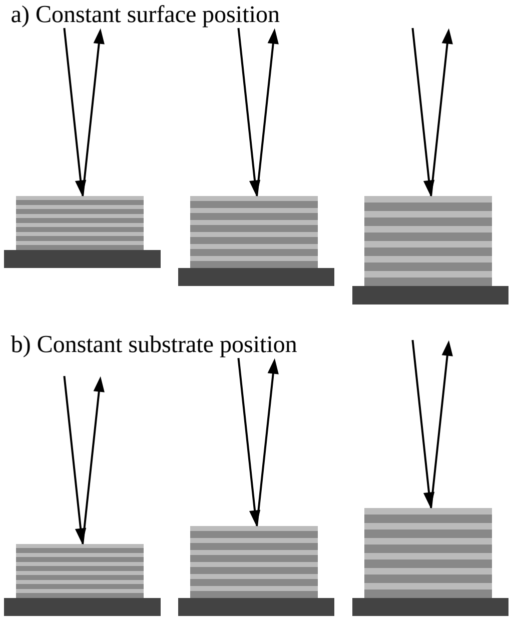

Figure 3. Two models for studying multilayer reflectivity, relevant to fabrication and metrology. (a) When the top surface is measured with visible-light interferometry *after* multilayer deposition, this model isolates the reflected phase effects seen only by the EUV light. (b) When the substrate position is known *before* multilayer deposition, this model is useful in setting layer thickness tolerances: Here the geometric path-length change and the reflected phase change are combined.

Consider two related models to describe this effect. These are shown in Figs. 3(a) and 3(b) First, the *constant surface position* model assumes that the position of the top-most layer surface is fixed in space. Here the measured phase variation with changing layer thickness is the same as the empirical expression given in Eq. (11). The relevance of this model comes from the comparison of visible-light and EUV interferometric measurements of the same optical system. With the assumption that the visible-light measurements are sensitive only to the position of the top surface, the difference between the two measurements is related to the thickness-dependent phase effects that are only observable *at-wavelength (*with EUV light).

Second is the *constant substrate position* model. When interferometric characterization is performed *prior* to the deposition of the multilayers, then the final surface profile may be inferred from the predicted multilayer coating thickness. Thickness errors in this model contribute both a geometric path-length change *and* the thickness-dependent phase change. The net phase change ϕ is thus the sum of a geometric component $\phi_{geometric}$ and the reflected-phase component. For N bi-layers of a multilayer with period length d_o, the optical path length changes by twice the height of the stack on reflection. Defining

Δd as the change from the optimal thickness d_o, and removing a constant phase term gives

$$\phi_{geometric}\ [\text{waves}] = 2N\,(\Delta d)/\lambda. \tag{13}$$

The reflected phase is described by Eq. (11). Combining these gives the net phase change

$$\phi\ [\text{waves}] = 2N\,(\Delta d)/\lambda - 7.49\,(\Delta d/d_o). \tag{14}$$

d_o is roughly $\lambda/2$ — the empirical value calculated earlier is $\lambda/1.957$. Inserting this into Eq. 13 gives

$$\phi\ [\text{waves}] = (1.022N - 7.49)\,(\Delta d/d_o) \approx (N - 7.5)\,(\Delta d/d_o). \tag{15}$$

This important result has the following implications. First, the geometric and the reflection components partially compensate each other: they are nearly balanced when N is seven or eight bi-layers. Typically, 40 layer pairs are used. In that case ϕ [waves] $\approx 33.4\,(\Delta d/d_o)$, and the contribution from the geometric term is roughly 5.5 times larger than the reflection term. The second, serious implication of this result is the tight tolerance it places on the layer thicknesses. Here, for phase changes less than $\lambda/20$, the thickness must be controlled to ±0.15%. To achieve $\lambda/50$, the thickness must be controlled to ±0.06%. At this point in time, it is not entirely clear that such tolerances are achievable, or even measurable.

A.4 FRESNEL ZONEPLATE LENSES

The Fresnel zoneplate lenses used in EUV applications and studied interferometrically in this thesis are essentially binary holograms of simple singlet lenses. Consisting of a patterned absorber layer on a thin support membrane, these elements operate in transmission and behave similarly to their conventional refractive counterparts. The zoneplate consists of a circularly symmetric pattern of alternating transparent and opaque concentric rings. The ring spacing decreases with increasing radius, and light diffracted by the zoneplate is directed toward or away from one single point on axis, different for each diffracted order.

Several excellent sources exists with descriptions of zoneplate theory, behavior, and fabrication (Sussman 1960, Hecht 1987:445-57). This appendix is intended to provide only a few important highlights, following the notation of Hecht (1987). Consider a zoneplate designed for point-to-point imaging. The object distance ρ_0 and image distance r_0 are on opposite sides of the screen where the zoneplate is defined. This

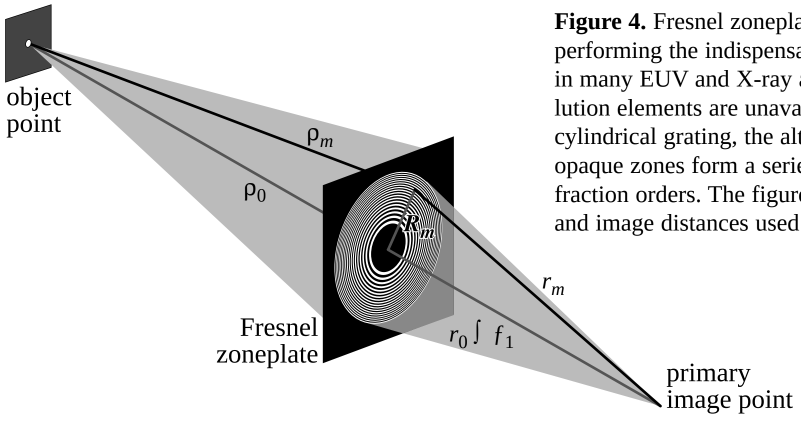

Figure 4. Fresnel zoneplate lenses operate by diffraction, performing the indispensable role of a simple refractive lens in many EUV and X-ray applications where other high resolution elements are unavailable. Essentially consisting of a cylindrical grating, the alternating pattern of transparent and opaque zones form a series of converging and diverging diffraction orders. The figure shows the definition of the object and image distances used in the zoneplate description.

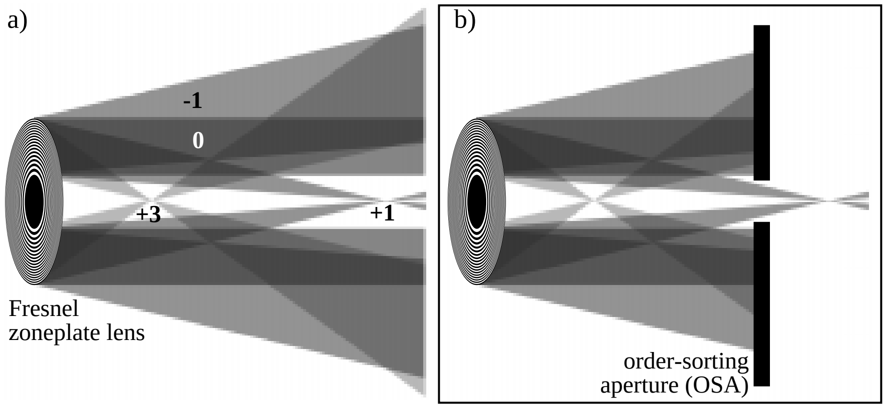

Figure 5. (a) A Fresnel zoneplate lens diffracts light into a series of converging and diverging diffraction orders. Only orders -1 through +3 are shown. Besides the “undiffracted” zeroth-order, even orders are absent. (b) Because of the overlapping orders, imaging applications usually require the use of an order sorting aperture that, if placed appropriately, can be used to transmit only the first-order converging light.

geometry is shown in Fig. 4. The individual zones are defined to diffract the diverging light from the object point to the primary image point in such a way that the light transmitted through each *open* zone adds *in phase*. Mathematically, this requirement indicates that the path-length difference between each open zone is λ; including the opaque zones, the path length difference between adjacent zones is $\lambda/2$.

$$(\rho_m + r_m) - (\rho_0 + r_0) = m\lambda/2. \tag{16}$$

With the zone radii defined as R_m, clearly $\rho_m = (\rho_0 + R_m)^{1/2}$ and $r_m = (r_0 + R_m)^{1/2}$. Assuming that the zoneplate radius is much smaller than the object and image distances and keeping only the first two terms in the expansions of ρ_m and r_m gives the relation

$$\left(\frac{1}{\rho_0} + \frac{1}{r_0}\right) = \frac{m\lambda}{R_m^2} . \tag{17}$$

Under plane-wave illumination, the object distance ρ_0 is extended to infinity. f_1 is defined as the primary focal length r_0, and the radius of the m-th zone is

$$R_m^2 = m f_1 \lambda . \tag{18}$$

Thus the zone placement radii are proportional to the square-root of m. For a given optical design, the main constraint on the size of the zoneplate is often dictated by the resolution limit of the zoneplate fabrication technique.

One important difference between the diffractive zoneplate and the conventional lens is the presence of numerous diffraction orders, as shown in Fig. 5(a). Analogous to the diffraction from a linear grating, a series of orders is diffracted into different directions; but in the case of the zoneplate, these multiple orders form a series of converging and diverging beams. The focal lengths f_m of the various beams occur at positive (converging) and negative (diverging) harmonics of the primary focal length.

$$f_m = f_1/m, \quad \text{for } m \in [\cdots\ \text{-}2, \text{-}1, 1, 2, \cdots], \text{ and } f_0 = \infty. \tag{19}$$

For a binary zoneplate, the even diffraction orders are absent.

When the zoneplate is used as a concentrating element designed to focus light to a certain point, other orders besides the first-order may often be ignored; their intensities are significantly less than that of the focused order at the primary focal position. However, in imaging applications, the various orders may suffer significant overlap, causing confusion in the recorded image. A practical remedy for this problem is the judicious placement of an *order-sorting aperture* (OSA) as shown in Fig. 5(b). When combined with an opaque central stop, as shown in the figure, the OSA may be placed in such a way that only the first-order beam is transmitted. The available space, or *working distance,* between the OSA and the primary focus may be smaller than is apparent due to the thickness of the OSA pinhole and the desire to provide as much longitudinal room near the focus as possible.

A.5 FRINGE CONTRAST AND MODULATION

The *contrast, modulation,* or *visibility* of a fringe pattern can be defined in several ways. These terms are used interchangably, and the definitions used in this thesis are presented here. A convenient description of an interference pattern separates the *stationary intensity* I_A from the *modulated intensity* I_B, with implicit spatial variation. Given a relative phase Φ between the amplitudes, the spatially varying intensity is

$$I = I_A + I_B \cos\Phi\ . \tag{20}$$

Since the intensity is non-negative, the average magnitude of I_A can never be less than that of I_B. When the electric field amplitudes of two interfering waves E_C and E_D are known, then neglecting the leading coefficients, the intensity can be written as

$$I = \left|E_C + E_D\right|^2 = \left|E_C\right|^2 + \left|E_D\right|^2 + 2\left|E_C E_D\right|\cos\Phi\ . \tag{21}$$

Hence, by equivalence to Eq. (20),

$$I_A = \left|E_C\right|^2 + \left|E_D\right|^2 \quad \text{and} \quad I_B = 2\left|E_C E_D\right|\ . \tag{22}$$

The *fringe modulation* γ is defined as the ratio of the modulated to the stationary intensities:

$$\gamma \equiv \frac{I_B}{I_A} \ \in\ [0,\ 1]\ . \tag{23}$$

Following Michelson, the fringe *visibility* or *contrast* is defined (Born and Wolf 1980:267) as

$$C \equiv \frac{I_{max} - I_{min}}{I_{max} + I_{min}}\ . \tag{24}$$

which, for the representation of the interferogram in Eq. (20), becomes

$$C = \frac{(I_A + I_B) - (I_A - I_B)}{(I_A + I_B) + (I_A - I_B)} = \frac{I_B}{I_A} = \gamma \ . \tag{25}$$

identical to the fringe modulation.

A.6 FOURIER-TRANSFORM METHOD OF FRINGE CONTRAST DETERMINATION

Fringe contrast plays an important role in the signal-to-noise ratio of the interferometric data (see Section 8.11). As a quantitative indicator of data quality (or system alignment), it is important to establish a consistent contrast measurement method. One simple method proposed here and applied throughout this thesis uses Fourier-domain analysis of the data to quickly compare the intensities of the zeroth- and first-order frequency components of the recorded intensity.

The application of this method closely parallels the Fourier-transform method of interferogram analysis, described in Chapter 11. The goal here is to determine the relative intensities of the zeroth- and first-order components of the spatial-frequency spectrum so that the fringe contrast may be found. Parseval's Theorem is invoked to relate the *energy content* of the spatial and spatial-frequency domain representations of the interferogram.

This method follows the spatial-frequency domain description of the interferogram presented in Section 11.3. The interferogram is represented as

$$I(\mathbf{r}) = A(\mathbf{r}) + B(\mathbf{r})\cos[\phi(\mathbf{r}) - \mathbf{k}_o \cdot \mathbf{r}], \quad \text{with } A,\ B, \phi\ \in\ R\ . \tag{26}$$

For the purposes of this discussion, the following simplification is useful:

$$I(\mathbf{r}) = A + B\cos[\phi(\mathbf{r}) - \mathbf{k}_o \cdot \mathbf{r}] . \tag{27}$$

A and *B* here are not actually constant, but may be considered to have only low-spatial frequency attributes. To facilitate the Fourier-domain representation of the interferogram, the cosine may be separated as follows:

$$I(\mathbf{r}) = A + \tfrac{1}{2} B e^{i\phi(\mathbf{r})} e^{i\mathbf{k}_o \cdot \mathbf{r}} + \tfrac{1}{2} B e^{-i\phi(\mathbf{r})} e^{-i\mathbf{k}_o \cdot \mathbf{r}} = A + C(\mathbf{r}) e^{i\mathbf{k}_o \cdot \mathbf{r}} + C^*(\mathbf{r}) e^{-i\mathbf{k}_o \cdot \mathbf{r}} , \tag{28}$$

where

$$C(\mathbf{r}) \equiv \tfrac{1}{2} B e^{i\phi(\mathbf{r})} , \tag{29}$$

and * indicates the complex conjugate. By inspection, the Fourier-transform of the interferogram may be written

$$i(\mathbf{k}) = a(\mathbf{k}) + c(\mathbf{k} - \mathbf{k}_o) + c^*(\mathbf{k} + \mathbf{k}_o) , \tag{30}$$

where $a(\mathbf{k})$ is approximately equal to $A\delta(\mathbf{k})$.

Now, similar to the Fourier-transform method, the zeroth- and first-order peaks are isolated from the rest of the spectrum, but here the *energy content* within a spatial-frequency radius κ is the quantity of interest.

The same assumptions about the separability of the peaks are made as with the Fourier-transform method of interferogram analysis. By Parseval's Theorem (Born and Wolf 1980:385, Goodman 1988:10), the zeroth-order components of the spatial and spatial-frequency domains are related.

$$\int |A|^2 \, d\mathbf{r} = \int |a(\mathbf{k})|^2 \, d\mathbf{k} \, . \tag{31}$$

Within κ, the approximate relationship holds

$$A^2 \propto \int_{|\mathbf{k}|<\kappa} |a(\mathbf{k})|^2 \, d\mathbf{k} \, , \tag{32}$$

and the constant of proportionality is simply $\int d\mathbf{r}$. A is found from the square-root of the expression in Eq. (32). The first-order term is now found in a similar manner. Once again invoking Parseval's Theorem,

$$\int \left| \tfrac{1}{2} B e^{i\phi(\mathbf{r})} \right|^2 d\mathbf{r} = \int |c(\mathbf{k})|^2 \, d\mathbf{k} \, . \tag{33}$$

This allows us to write

$$\left(\tfrac{1}{2} B\right)^2 \int d\mathbf{r} = \int_{|\mathbf{k}|<\kappa} |c(\mathbf{k})|^2 \, d\mathbf{k} = \int_{|\mathbf{k}-\mathbf{k}_o|<\kappa} \left|c\left(\mathbf{k}-\mathbf{k}_o\right)\right|^2 d\mathbf{k} \, . \tag{34}$$

To within the same constant of proportionality as for A ($\int d\mathbf{r}$), B can be found

$$B \propto 2\left(\sqrt{\int_{|\mathbf{k}-\mathbf{k}_o|<\kappa} \left|c\left(\mathbf{k}-\mathbf{k}_o\right)\right|^2 d\mathbf{k}} \right). \tag{35}$$

The factor of two comes from the definition of B and from the fact that the energy in the first-order is divided equally between the equivalent symmetric peaks in the spatial-frequency domain.

Since, by assumption, the three components of the spatial-frequency spectrum are separable, the expressions for A and B can be re-written using $i(\mathbf{k})$. The ratio of B to A gives the scalar *global fringe contrast* for an interferogram.

$$contrast = 2 \sqrt{ \frac{ \int_{|\mathbf{k}-\mathbf{k}_o|<\kappa} |i(\mathbf{k})|^2 \, d\mathbf{k} }{ \int_{|\mathbf{k}|<\kappa} |i(\mathbf{k})|^2 \, d\mathbf{k} } } \, . \tag{36}$$

This expression is easily implemented on a computer. Using the standard mathematical Fast Fourier Transform (FFT), locating the first-order peak (i.e. determining $\mathbf{k}_o$) proceeds by searching for the maximum absolute value in a region that excludes the central, zero-frequency peak. An exclusion radius of 30 cycles was chosen for typical EUV PS/PDI interferograms but would be different if a smaller sub-region of the data were being evaluated. Depending on the combined characteristics of the illuminating beam and of the test optical system, a small radius must be chosen that is large enough to encircle nearly all of the zeroth- or first-order components in the spatial-frequency domain. To avoid overlap, this radius must not be larger than half of the "distance" between the first-order peak and the central frequency. A radius of ten cycles was chosen for these EUV interferometry experiments.

A.7 READING ZERNIKE COEFFICIENT PLOTS

Throughout this thesis, wavefront phasemap data is represented using the coefficients of the first 37 terms of the Zernike polynomial series, representing the best fit surface to the data. As described in Chapter 14, each term represents one orthogonal aberration polynomial component. Of the first 37, there are seven cylindrically symmetric terms and fifteen pairs of terms that share the same radial dependence but have cos($m\phi$) and sin($m\phi$) angular dependence.

Figure 6 is designed to serve as a *key* for identifying the various polynomial terms from the Zernike coefficient plots. For the PS/PDI data, the first four Zernike polynomial components are the position-dependent terms which depend only on the measurement and *not* on the optic under test. These are the *piston, tilt,* and *defocus* components, and they are typically excluded from the graphs.

Note that there is no significance to the line that connects the individual points in the plot. Its presence only aids in distinguishing one point from the next.

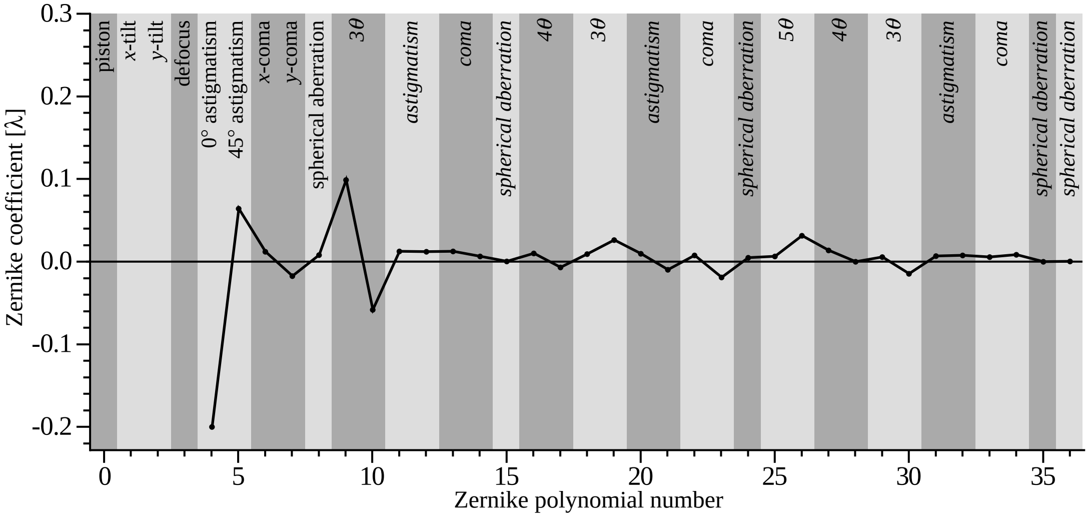

Figure 6. Key to Zernike coefficient plots. Here the named and unnamed components of a Zernike polynomial series are identified on the graph. Individual terms and pairs of terms that share radial dependence are identified by the grey vertical bands. The Zernike polynomials are described in Chapter 14. The line connecting the individual points of the discrete set has no physical significance.